Stall Control by Plasma Actuators: Characterization along the Airfoil Span

Giulia Zoppini [1], Marco Belan [2],*, Alex Zanotti [2], Lorenzo Di Vinci [2] and Giuseppe Campanardi [2]

[1] Department of Aerodynamics, TU Delft, Leeghwaterstraat 42, 2628 CA Delft, The Netherlands; g.zoppini@tudelft.nl

[2] DAER, Politecnico di Milano, Via La Masa 39, 20156 Milano, Italy; alex.zanotti@polimi.it (A.Z.); lorenzo.divinci.ldv@gmail.com (L.D.V.); gabriele.campanardi@polimi.it (G.C.)

* Correspondence: marco.belan@polimi.it

Abstract: A dielectric barrier discharge actuator (DBD) is considered and studied as a stall recovery device. The DBD is installed on the nose of a NACA0015 airfoil with chord $\times$ span 300×930 mm. The geometry of the exposed electrode has periodic triangular tips purposely designed for the case under study. Wind tunnel tests have been carried out over a range of airspeeds up to 35 m/s with a Reynolds number of 700 k. The flow morphology has been characterized by means of the particle image velocimetry technique, obtaining velocity fields and pressure coefficients. By exploring different planes along the model span, the three-dimensional effect of the DBD has been reconstructed, identifying the flow region mainly sensitive to the plasma actuation. Finally, the actuator effectiveness has been quantified accounting for the power consumption data, leading to defining further design improvements in view of a better efficiency.

Keywords: flow control; separation control; plasma actuators; dielectric barrier discharge

1. Introduction

The research on plasma actuators begun only a few decades ago, but it rapidly spread thanks to the very good performance demonstrated by these devices. In particular, in recent years, a constantly increasing interest developed in the application of DBD (Dielectric Barrier Discharge) actuators in the flow control field [1,2]. In the standard configuration, they consist of two electrodes separated by a layer of dielectric material. By applying an alternating voltage between them, they induce a streamwise velocity component that accelerates the airflow in the vicinity of the wall they are mounted on. As a consequence, the boundary layer can be manipulated in several ways, depending on the DBD application. A detailed description of their working principles is reported in References [2–4].

Their rapid diffusion in the aeronautical field is mainly due to their capability to directly convert the supplied electric energy into kinetic energy without involving moving mechanical parts. This reduces their weight with respect to classical flow control devices, making them simple to assemble and modify. Moreover, even their response time is better, enabling high-frequency real-time control applications. Some studies are still performed to improve their efficiency in energy conversion.

Plasma actuators, and more specifically DBD, have already controlled flows for Reynolds numbers above 10^6 [5]. They have different control capabilities depending on their geometry and applications. When applied to control stall on an airfoil, they are usually installed upstream of the expected separation point [6]. In this way, separated flows [7], shear layers [8], and boundary layer laminar-to-turbulent transitions [9] were successfully manipulated. If aligned with the freestream, they behave as vortex generators, with the advantage of being operated only when needed. Furthermore, their control performance can be improved through a burst modulation of the voltage

signal, especially when dealing with a deep stall configuration [6,7,10], provided that the wave frequency and duty cycle are properly chosen [11]. Recent studies demonstrated that nanosecond pulsed DBD, with their very low active time, can manipulate separation for Reynolds numbers even above 2×10^6 [12]. If located near the trailing edge, plasma actuators can behave as flaps increasing the lift coefficient [6,13].

The DBD actuator performance can be enhanced through the optimization of the input signal [2,14] or of the exposed electrode geometry that can be specifically designed for each particular application [15]. Sharp tips are known to increase ionic wind and thrust [14], inducing also transverse velocity components that give rise to streamwise vortex structures [16], so that their interaction with the flow field improves the boundary layer mixing and the actuator control capabilities. The present research, focused on a stalled airfoil, deals with the flow modifications due to a DBD with multiple triangular tips, regularly spaced [17–21].

Many of the researches on plasma actuators are dedicated to their applications on airfoils or exploit airfoils as test cases. In most cases, the plasma–flow interaction is only characterized in correspondence with the central sections, implicitly performing a two-dimensional analysis on a flow that is actually three-dimensional. Only a few studies, such as References [6,12], introduce large end-plates or other purposely designed devices that counteract the development of three-dimensional flow structures. The present work follows instead an opposite approach: to allow the complete development of the three-dimensional structures that naturally characterize the aerodynamic flow field, the airfoil model is intentionally not provided with end-plates. Accordingly, in this work, the DBD test is performed inherently accounting for the flow three-dimensionality, characterizing the plasma-flow interaction all along the airfoil span. This is achieved by repeating PIV measurements on different spanwise distributed planes. In turn, this allowed to identify the flow region most affected by the actuator, suggesting some design modifications that can improve the device efficiency.

This work at first describes the experimental setup and its validation through PIV measures performed on the central sections. Then, it focuses on the analysis of the spanwise distributed sections, characterizing the actuator influence on the three-dimensional flow. Finally an approximated estimation of the actuator efficiency is reported.

2. Experimental Setup

2.1. Airfoil

The main element of the setup is the wing model purposely built for this experiment, with span $S = 930$ mm, constrained by the test section width, and chord $c = 300$ mm. A NACA0015 airfoil was chosen because it has been widely used in literature about plasma actuators tests, becoming a standard in this field (References [6,8,10,11,22] are just a few examples). As exposed in the Introduction section, no end-plates were integrated in order to allow a complete development of the relevant three-dimensional flow that is not negligible despite the relatively good aspect ratio $S/c = 3.1$. The flow pattern cannot be considered identical to the one obtained in unbounded streams; however, the gaps between wing tips and lateral walls, equal to 35 mm ≈ 0.12 c, are large enough to allow the desired study of the three-dimensional flow. In fact, it is reported that very small gaps, in the order of 0.005 c, already give visible effects on the streamlines pattern that may affect also the centerline flow [23]. As shown in the Results section, the larger gaps used in this experiment lead to a separated region similar to the so-called mushroom stall cell observed by testing wings in free-jet facilities [23]. As a consequence, the boundary of the separated region in this experiment becomes a curved line on the airfoil surface, well known in literature, where the phenomenon is documented for several airfoils including NACA 0015, even if it mainly depends on the aspect ratio [24–26].

The model is realized in ureol, a polyurethane foam extremely rigid and electrically insulating. It is completed by two side ribs and two tubular shafts that permit to couple it with a supporting structure that allows to set the angle of attack and firmly holds the airfoil during tests. On one side, the

rib and shaft are made of nylon to improve the insulation because the high voltage cable is clamped on them during the tests. On the opposite side, the components are made of aluminium alloy to improve the pitching constraint. The whole airfoil + shafts assembly is shown in Figure 1.
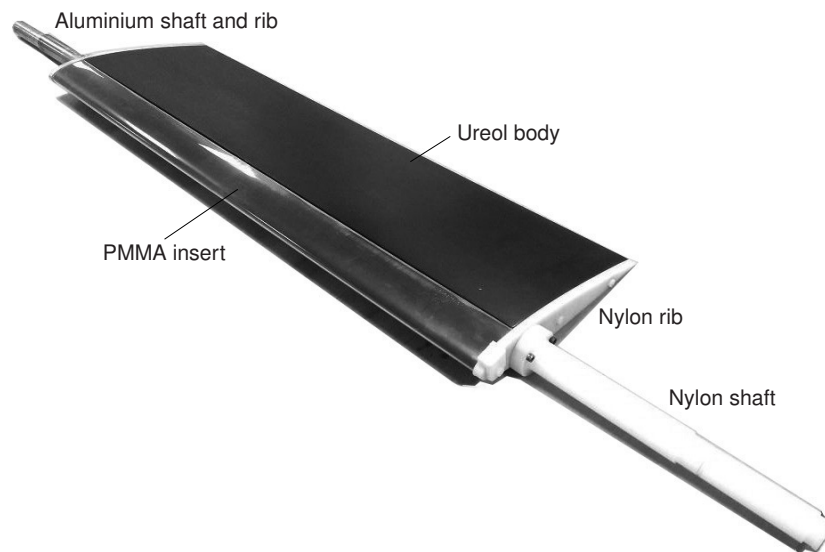

Figure 1. NACA0015 assembly.

2.2. Wind Tunnel and PIV Setup

The PIV measurements were performed in the "Sergio De Ponte" wind tunnel, a closed circuit facility with a $1.5 \times 1 \times 3$ m test section. The nominal power is 100 kW, allowing airspeeds up to 55 m/s in the test section, which is optimized for aeronautical purposes, with a turbulence level lower than 0.3% and streamlines with angular variations lower than $0.1°$. The model and the instrumentation have been assembled on a test rig derived from a previous experiment designed to bear high aerodynamic loads [27]. In order to evaluate the complete flow field over the suction side of the airfoil, it was necessary to install two PIV cameras, each one with a 2 Mpx CCD sensor, rigidly constrained to the support structure. They were fitted with two different lenses, a 50 mm one on the fore camera in order to obtain an higher definition on the leading edge (DBD region) and a 24-mm lens on the aft camera to have a wider flow field on the mid-rear section of the airfoil. The laser system originates impulses of 200 mJ with 532 nm wavelength and was synchronized with the cameras. Wind seeding was obtained by dispersing Di-Ethyl-Hexyl-Sebacate (DEHS) droplets. The complete setup is sketched in Figure 2, and a sample of the fields covered by the two cameras is shown in Figure 3.
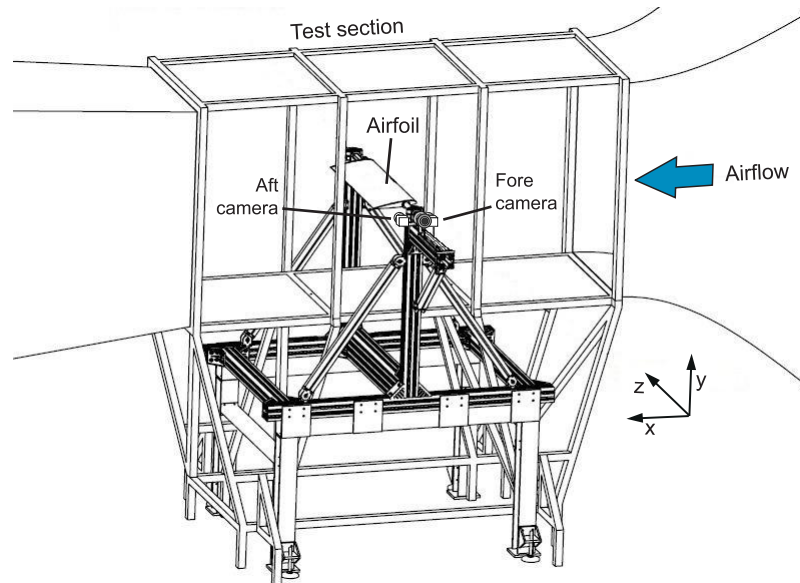
Figure 2. Wind tunnel setup: The laser sheet enters the test section from below.

Figure 3. Sample PIV fields of the two cameras with their overlap, shown by means of two original images: The image domains are adjusted separately in different tests, when the PIV plane is moved spanwise or when the angle of attack is changed.

2.3. DBD Actuator

The most complicated part of the setup phase was the geometrical optimization of the DBD, assembled on the PolyMethyl Methacrylate (PMMA) insert of Figure 1. The first design choice regarded the exposed electrode shape: equally spaced nonadjacent triangular tips were chosen since each tip can induce a locally high ionic wind injecting streamwise momentum, and at the same time, the transverse induction between tips can generate vortex structures [14,17,19,20]. Other shapes with periodic contours such serrated, serpentine, and square wave have been described in literature [16]; however, the adjacent tips of a standard serrated shape do not allow to set the proper space for optimal development of vortex structures, whilst serpentine and square shapes cannot create local streamwise jets as separate triangular tips do. Another well-studied shape is the plasma vortex generator, an array of streamwise-oriented linear DBDs [26]; this is optimized for creating vortex pairs but not capable of adding direct streamwise momentum to the flow.

The specific properties of the present DBD are described in what follows. The shape of a single triangular tip is completely defined by setting its length h and base width w. Then, the ratio $r = h/w$ (tip sharpness) can be defined to characterize it: values of r higher than 1 give progressively higher electric fields and induced velocities, but excessive values can favour the formation of electric arcs or excessive heat that damages the device. The above considerations and the outcome of some bench tests

led to set a sharpness $r = 5$. This *tip effect*, also known for corona actuators [27,28], enhances the stall control but is known to scale with U_∞^{-2}, progressively losing intensity as the freestream velocity is increased [20]; however, to keep a better authority on the flow at higher velocities, the sharp tips can be separated by a suitable inter-tip spacing d. Thanks to the orthogonality of the induced velocity to the electrode perimeter, in the gaps between adjacent tips, opposite transverse motions are created, giving rise to pairs of counterrotating vortex structures. This improves the boundary layer mixing, so that, with this geometry, the actuator behaves also as a vortex generator (VG), as described in Reference [17,29] and as sketched in Figure 4 in plane form.
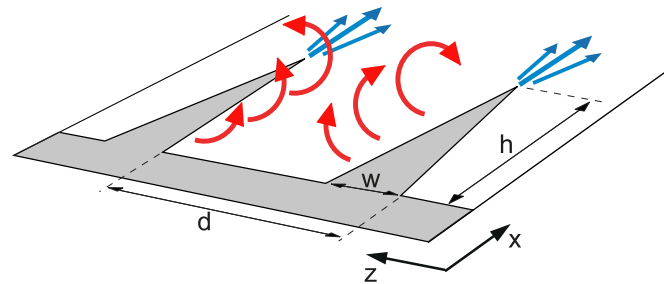

Figure 4. Sketch of the effects of triangular tips on the exposed electrode: momentum injection (blue) and vortices generation (red).

If the tip spacing is suitably chosen, this effect significantly enhances the actuator authority. In literature, the optimal spanwise spacing for a plasma vortex generator has been found to depend only on the discharge length, independently of the incoming boundary layer thickness [26]. The optimal spacing turned out to be twice the discharge length, in such a way as to permit the right development of a double plasma sheet between adjacent elements (between adjacent tips in the present shape). To check this property and to determine a suitable spacing d for the present application, some bench tests were conducted following the method described in Reference [30]. The available power supply of $40\,\mathrm{kV}_{pp}$ gives a discharge length of 18 mm, and this led to setting a tip spacing of $d = 36$ mm.

In this DBD geometry, the last important parameter is the tip length h, that required a further analysis, strictly linked to the airspeed U_∞. This relation is based on the study of the formation and evolution of the streamwise vorticity ω_x, crucial for the correct working of a VG. The generation of ω_x vorticity was at first investigated for low freestream values in Reference [31]; then, its characterization was extended at higher velocities in Reference [26]. To design the present actuator, the x-component of the vorticity transport equation was dimensionally analyzed [20], confirming that the VG effect is due to a reorientation of the large spanwise vorticity ω_z carried by the approaching boundary layer. This process gives rise to the ω_x component but requires a minimum residence time of the fluid particles over the electrode to effectively occur. The main time scale is the convective time, defined as $T_C = h/U_\infty$ along the tip length h; instead, the viscous scale $T_\nu = \delta^2/\nu$, based on the thickness δ of the approaching boundary layer, turns out to be much longer, namely $T_\nu \gg T_C$, so that an inviscid analysis is satisfying. To quantify the reorientation time, it can be considered that the vortex structures lay within the boundary layer (their size is enlarged for clarity in Figure 4). Then, the VG effect implies that a fluid particle of the external flow that travels along the actuator is pushed toward the wall while it rotates around the streamwise direction. The velocity of the transverse (spanwise) motion can be assumed in the order of the ionic wind V_i (less than 5 m/s), and the particle can be considered to sweep transversally almost half the inter-tip spacing d. Thus, the recirculation time scale can be defined as $T_R = d/(2V_i)$, and to allow a complete vorticity reorientation, the primary time constraint becomes $T_C \geq T_R$ or, at least, of the same order of magnitude. This means that a fast fluid particle traveling along the DBD has enough time to be dragged toward the wall before leaving the electrode zone.

For this application, the value of h was initially estimated considering a freestream velocity of $U_\infty = 20$ m/s so that, accounting for the time scales described above, the tips length was set to

$h = 50$ mm. At the same time, this value is compatible with the overall model dimensions. Afterwards, during the test campaign, the actuator demonstrated a very good authority and was tested also at higher freestream speeds, showing significant control capabilities on the flow up to $U_\infty = 35$ m/s. Thanks to these results, the spanwise tests were performed at the intermediate velocity of $U_\infty = 30$ m/s, at which the $T_C \geq T_R$ constraint is only approximately satisfied but the Reynolds number reaches the value Re = 600 k, closer to the ones of aeronautical interest.

To summarize the electrode design procedure, the availability of a 40 kV_{pp} power supply led to the geometry visible in flat form in Figure 5, where $d = 36$ mm, $h = 50$ mm, and $w = 10$ mm. With 22 tips, the overall electrode span is $S = 756$ mm, tip-to-tip. This electrode was applied on the external surface of the C-Shaped PMMA sheet, as shown in Figure 6, and a 800 × 60 mm ground electrode was applied on the inner surface. Both of them are manufactured from a 125 μm thick aluminium foil.
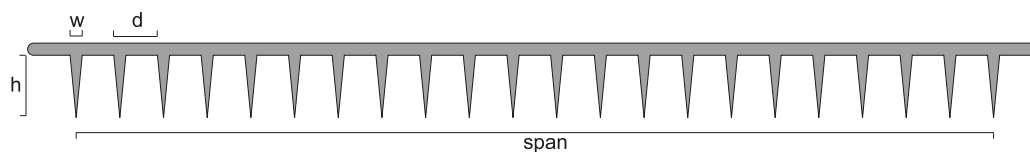

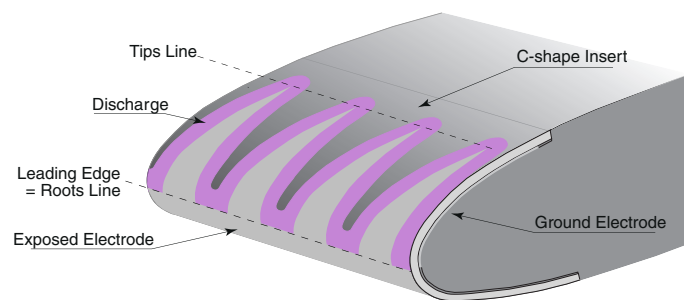**Figure 5.** Exposed electrode geometry.

Figure 6. Section of the dielectric barrier discharge (DBD) actuator, assembled on the airfoil and seen from below of Figure 2: The discharge is sketched as a color band around the contour of the exposed electrode. At maximum voltage, the discharge fills almost completely the spaces between tips.

The DBD can be operated in steady mode by supplying a sinusoidal waveform or in pulsed mode by supplying repetitive wavetrains (a sinusoidal carrier modulated by a square wave). Before being mounted in the test section, the assembled model was tested at bench to determine the actuator power requirements. The supply chain is composed by a signal generator, a precision potentiometer, an amplifier, and a transformer. The last element has been specifically designed for this application to generate a maximum output voltage of 14.12 kV$_{eff}$ corresponding to 40 kV$_{pp}$ and to manage a power of 250 W. The measures at the bench were performed to determine the power requirements at the worst conditions, i.e., with steady actuation (carrier frequency f without modulation). The dependence of power on the carrier frequency f has been determined while keeping a fixed voltage in order to choose an input signal that optimizes the actuator performance keeping at the same time safe conditions for the instruments. With 40 kV$_{pp}$, a progressive increase of the frequency led to measure a power of 195 W on the primary winding at $f = 650$ Hz. This power, close to 80% of the allowed maximum, was considered safe for the supply chain and then was fixed for the wind tunnel tests. Under these conditions, the power actually fed to the actuator was measured on the secondary winding side, giving 167 W. This corresponds to a transformer efficiency of 0.86 that turned out to be nearly constant over the range 300 to 650 Hz.

3. Results

In this section, the results of the PIV analysis are presented, beginning with the study of the central sections at the design velocity of U_∞ = 20 m/s. Through these measures, the setup was validated and the DBD effect was tested. Successively, the freestream speed was increased to U_∞ = 30 m/s and the actuator effect was studied over the whole wing, considering several spanwise sections. Figure 7 reports a sketch of the actuator and of the PIV measurement planes. In what follows, the term *root* indicates the middle point of the inter-tip spacing, namely the one at $d/2 = 18$ mm from each tip, as shown by the yellow line in Figure 7.
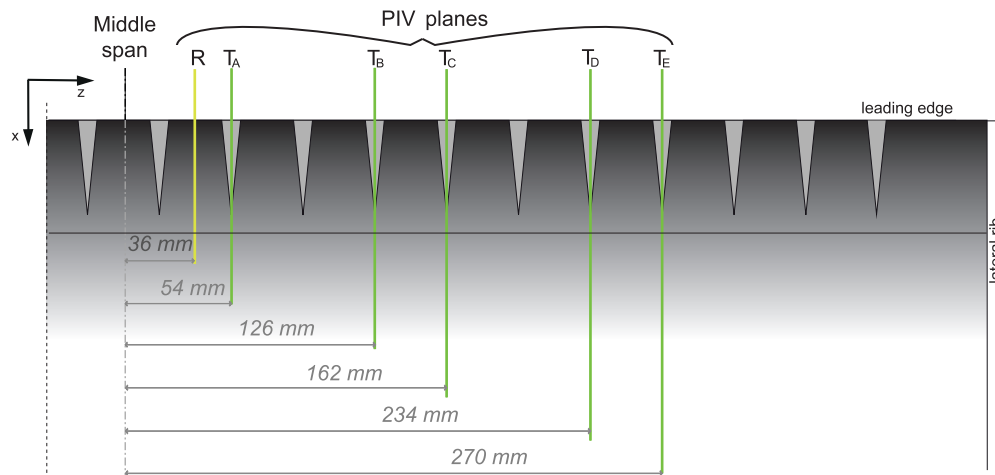

Figure 7. Sketch of the exposed electrode geometry with PIV measurement planes, seen from below in Figure 2.

3.1. Central Sections Analysis at $U_\infty = 20$ m/s

The first measures were performed on the central sections as usual for this type of investigations, starting from tip T_A. This PIV plane was initially studied in early stall conditions, with an angle of attack $\alpha = 14.5°$ at the design velocity of U_∞ = 20 m/s. The actuator was supplied with a steady sinusoid of frequency $f = 650$ Hz. Here and in all the PIV measurements, the mean flows are obtained by averaging on a suitable time scale at least 100 velocity fields obtained by corresponding pairs of images. All the PIV planes are shown on a xy domain with the origin on the leading edge, made dimensionless with respect to the chord c and its projection $c' = c \cos \alpha$.

Figure 8a shows the plasma-off mean flow field. A recirculation bubble is present and extends up to the trailing edge. The separation starts at about 30% of the chord, and the relevant point is represented here and in all of the reported mean flow fields by a red arrow.

The separation is detected by an approximation method, as follows. First, a zoomed-in field of the relevant flow region is built in order to obtain a detailed representation of the local streamlines, consistent with the PIV resolution. Among these streamlines, the algorithm identifies the one which is approached by the wall flow on both sides with opposite directions. This streamline is assumed to start from the separation point on the wall; however, this procedure cannot describe the boundary layer details, so this streamline is identified only outside the boundary layer, up to a small distance from the airfoil and then extended through extrapolation until it intersects the solid surface. The point identified in this way is considered as a suitable approximation of the separation point: the introduced error is considered acceptable since the final aim is that of defining the relative modification of the flow comparing the plasma-on and plasma-off configurations and not the absolute locations of the separation points.

In the plasma-on configuration, Figure 8b, a strong shift in the separation point and a significant reduction of the recirculation bubble can be seen. Under the plasma effect, they are both confined

to a region of about one quarter of chord from the trailing edge. The streamline acceleration is quite evident too: they are deflected toward the airfoil. These modifications are expected to be beneficial for the local pressure and lift coefficients, C_P and C_L. Besides, since the wake of the airfoil is strongly reduced, a decrease of the drag coefficient can be expected too.
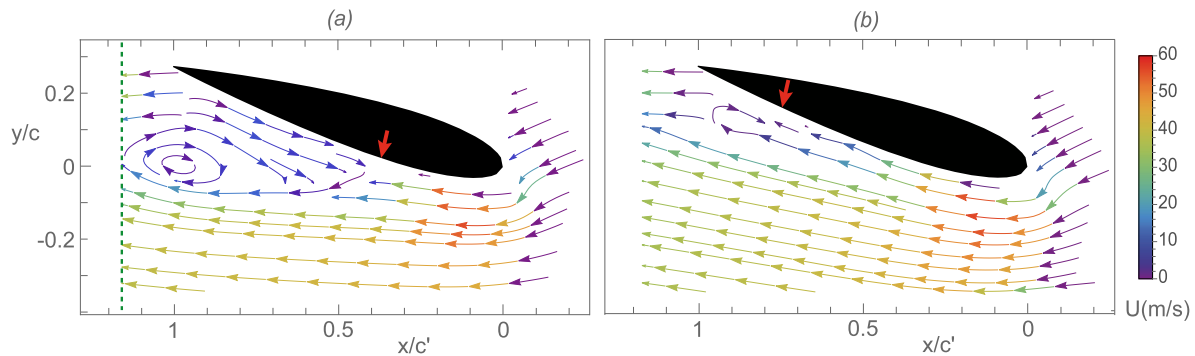

Figure 8. (**a**) Plasma-off and (**b**) plasma-on flow field at T_A for $\alpha = 14.5°$ and $U_\infty = 20$ m/s: The dashed line in panel a marks the position of the cross-wake velocity profiles presented in Figure 9.

These effects are confirmed by the analysis of the cross-wake velocity profile and the estimation of C_P, reported in the two following graphs. The former, Figure 9a, allows to compare two velocity profiles in the wake, corresponding to plasma-off and -on configurations. This and all the cross-wake velocity profiles are obtained retrieving the velocity values along an axis located at $c/6 = 50$ mm downstream of the trailing edge, evidenced in Figure 8a. Within the measurement domain, this location allows to determine mean values in a region less unsteady than the close proximity of the airfoil. As expected, in the upper and lower part of the domain, the velocity values are almost coincident with the freestream ones, while a momentum drop is visible in correspondence with the wake region. It can be noted, though, that, in the actuated case, represented by the red curve, the momentum drop is significantly reduced along with the region it interests. This contributes to the thinning of the wake and the reduction of its blockage. It should also be outlined that, in the upper part, the two curves do not coincide perfectly: the plasma-on case shows a lower velocity with respect to the plasma-off one. This may be explained considering that the actuator can affect the whole flow around the airfoil, modifying the circulation and the stagnation point position on the pressure side, which is indeed in the upper part of the figure.
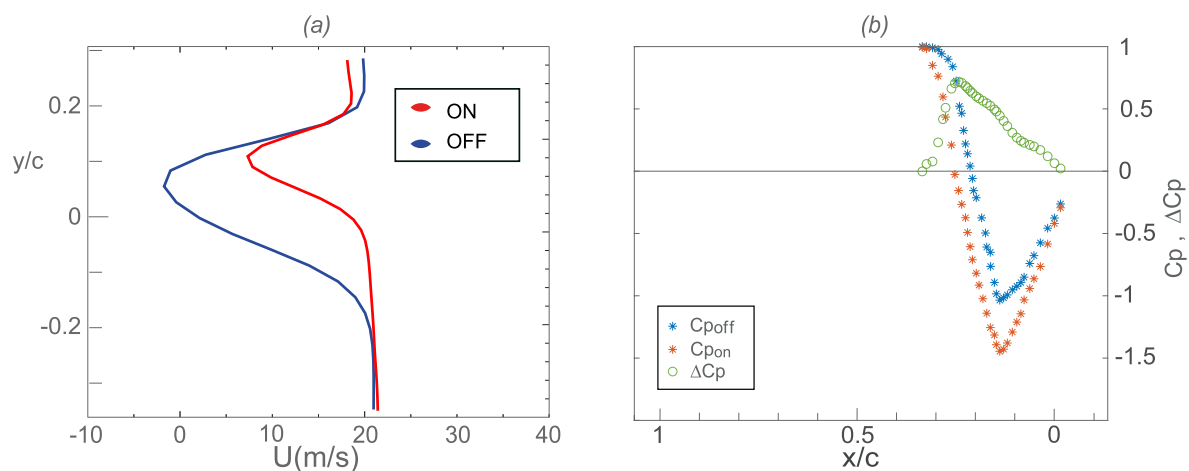

Figure 9. (**a**) Cross-wake velocity profile and (**b**) C_P values at T_A for $\alpha = 14.5°$ and $U_\infty = 20$ m/s.

An estimation of the C_P was obtained through suitable elaboration of the collected PIV data. This calculation was performed applying the Bernoulli theorem to the attached flow areas, namely beginning from the proximity of the leading edge and stopping the evaluation in the separation zone. Through this simplified procedure, only an approximation of the coefficient was obtained: for the PIV field of Figure 8, it is reported in Figure 9b, where a significant off-to-on growth of the C_P peaks in the order of 35% is observed. Unfortunately, this estimation can hardly be compared with experimental or numerical reference data since it is known that narrow C_P peaks are difficult to obtain from PIV data because of resolution limits that easily lead to underestimate the desired value [32]. In fact, the peak is related to the maximum over-speed of the flow, of which the values are usually found in a small region very close to the airfoil that would require a locally very fine grid of PIV data to be properly resolved. However, the same order of approximation affects both the on and off configurations, so that the off-to-on variations can be considered here to give further information about the actuator capabilities for given conditions of airspeed, angle of attack, and spanwise position.

Both the effects of vortex generation and momentum injection strongly influence the flow around the airfoil. As described in Section 2, the direct momentum injection is principally due to the tips thanks to the high local electric field they develop. The inter-tip spacing, instead, is characterized by the presence of the vortical structures. This induces different local modifications on the flow that are evidenced in the following analysis through the description of the measures performed at the same $\alpha = 14.5°$ and $U_\infty = 20$ m/s conditions on the root plane R.

In Figure 10a, that represents the root plane with plasma off; the flow is quite similar to the one at the tip, indicating that the passive effect of the unpowered actuator is quite weak at this Reynolds number and can be neglected. Instead, in the plasma-on case of Figure 10b, the shift in the separation point appears to be milder as is the streamlines acceleration effect. This may be explained considering that, at the root plane. the ionic wind has also a component orthogonal to the wall and directed toward the external flow, whereas the tips induce a wind almost parallel to the wall. Moreover, the induced velocity at T_A is generated in a downstream chordwise position with respect to the roots. Considering that the reduction of the recirculation bubble is significant also at the root R, it can be concluded that the local flow pattern generated by the actuator keeps trace of the shape of the exposed electrode.
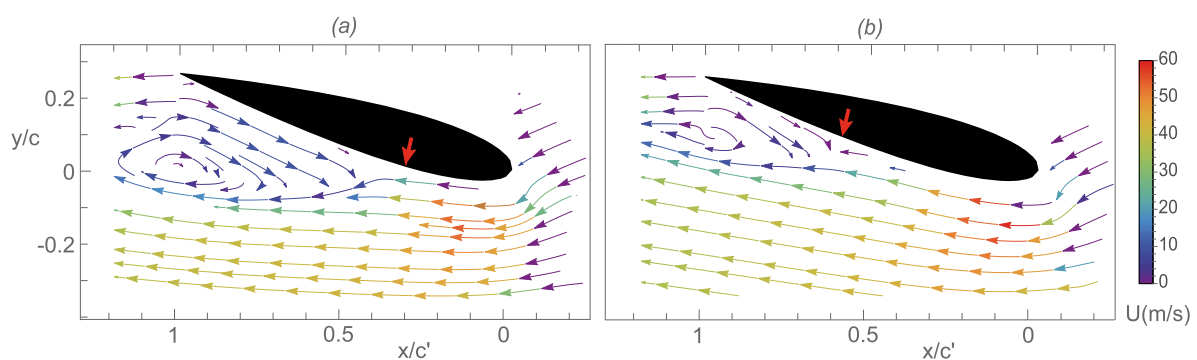

Figure 10. (**a**) Plasma-off and (**b**) plasma-on flow field at R for $\alpha = 14.5°$ and $U_\infty = 20$ m/s.

The cross-wake velocity profiles, computed as previously described and reported in Figure 11a, confirm the effectiveness of the actuator, showing a reduction of the momentum drop similar to the one downstream of the tip T_A in the actuated case; thus, the wake region appears to be less affected by the electrode shape. The pressure coefficient trends, visible in Figure 11b, are instead more influenced by the actuator shape, since the attached flow region is mainly located over the active electrode. In particular, the peak value of C_P exhibits only a slight increase in the plasma-on configuration, lower with respect to the one measured at the tip.
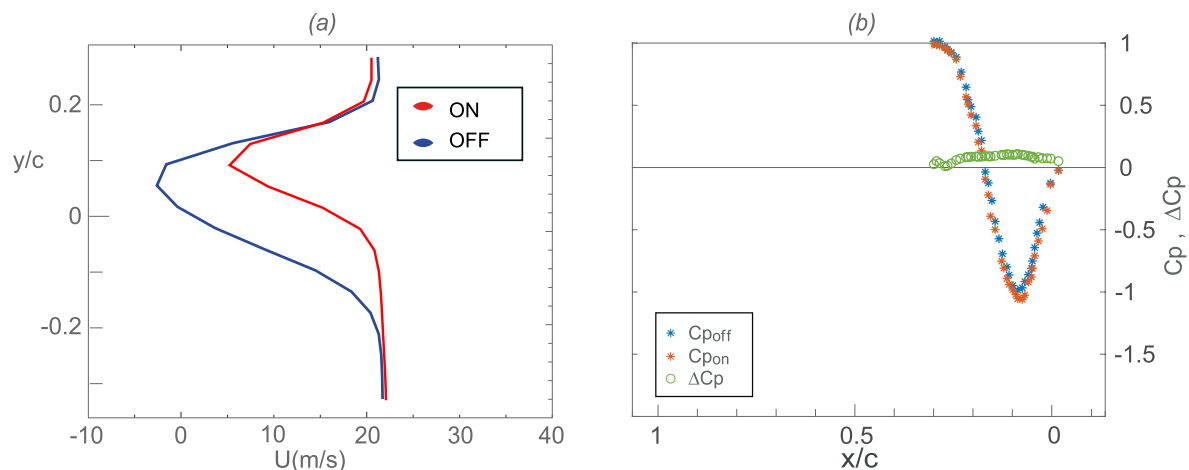
Figure 11. (**a**) Cross-wake velocity profile and (**b**) C_P values at R for $\alpha = 14.5°$ and $U_\infty = 20$ m/s.

To test the actuator under more challenging conditions, a deep stall configuration with an angle of attack $\alpha = 22°$ was introduced. Previous studies [7,22] underlined that, to exert an effective control on a deep stall, it is necessary to directly interact with the vortex structure formation and detachment. This is typically achieved by pulsing the actuation with a repetition frequency F close to the vortex shedding one. For a DBD, the pulse frequency F represents a square wave modulation applied to the normal (carrier) frequency f. The pulses repetition is usually expressed by means of the reduced dimensionless frequency F_+, defined in literature as $F_+ = F\,c/U_\infty$. Its most effective value for stall control is proved to be close to 1, corresponding to the time scale of a fluid element traveling along the chord c at velocity U_∞. Accordingly, also in this study, F_+ was set to unity while the carrier frequency f was kept at 650 Hz. Another important parameter is the duty cycle, which represents the (active time)/(pulse period) ratio, here, varied from 20% to 50%. Within this range, it does not significantly influence the effect of the actuator on the flow; however, lower values correspond to lower power consumptions.

In Figure 12a, the plasma-off condition is observed. It is characterized by a separation point laying close to the leading edge and a recirculation bubble much larger with respect to early stall, expanding also outside of the captured region. The actuator is not expected to reattach the flow, but the plasma-on configuration shows a mild shift in the separation point, still represented by the red arrow and a clearly visible change in the size and shape of the recirculation bubble (Figure 12b). Thanks to the pulsed actuation mode, the bubble is shifted closer to the airfoil and a well-visible recirculation structure appears.
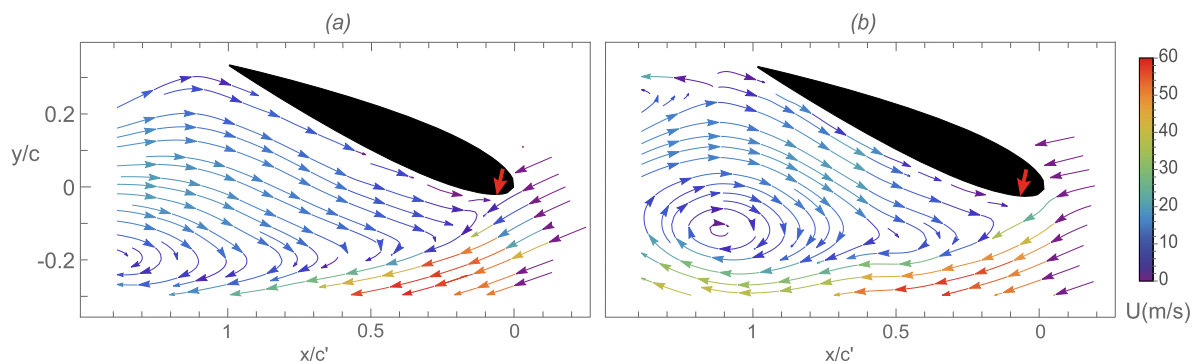

Figure 12. (**a**) Plasma-off and (**b**) plasma-on flow field at T_A for $\alpha = 22°$ and $U_\infty = 20$ m/s.

These modifications are once again confirmed by the cross-wake velocity profiles. In fact, Figure 13a indicates a significant reduction of the region interested by the momentum drop, even if the whole wake profile, remarkably large for $\alpha = 22°$, cannot be recovered by the present setup.
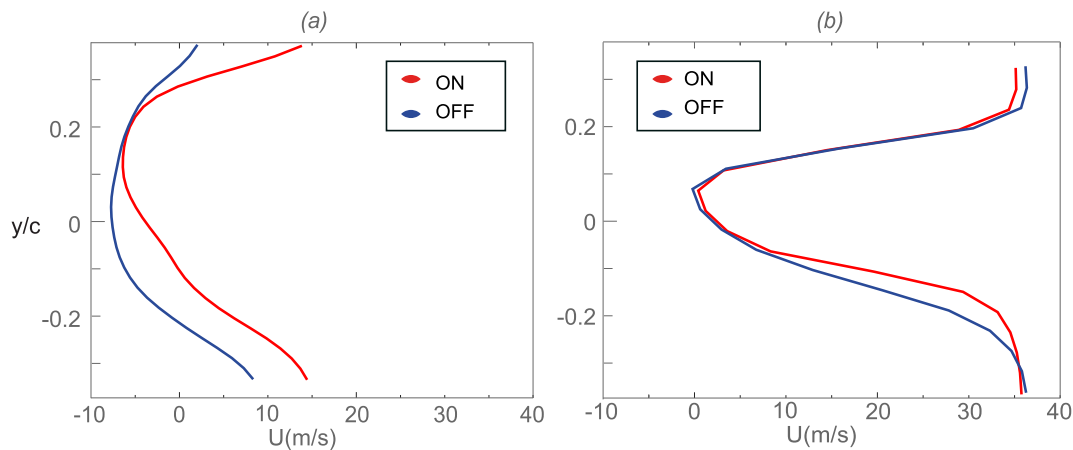
Figure 13. Cross-wake velocity profiles at T_A for (**a**) $\alpha = 22°$ and $U_\infty = 20$ m/s and (**b**) $\alpha = 14.5°$ and $U_\infty = 35$ m/s.

Further measures were carried out to find the maximum operational velocity at which the actuator still controls the flow. Its value turned out to be in the 35 to 40 m/s range at $\alpha = 14.5°$. The $U_\infty = 35$ m/s case is reported in Figure 14a,b, where a slight shift in the separation point and a reduction in the recirculation bubble are still visible. The flow modifications are better observed comparing the cross-wake velocity profiles reported in Figure 13b. They confirm the wake width reduction effect, and also in this, case the velocity of the two curves is slightly different in the proximity of the trailing edge, i.e., in the upper part of the graph. As previously stated, this is presumably due to the overall effect of the actuator on the circulation.
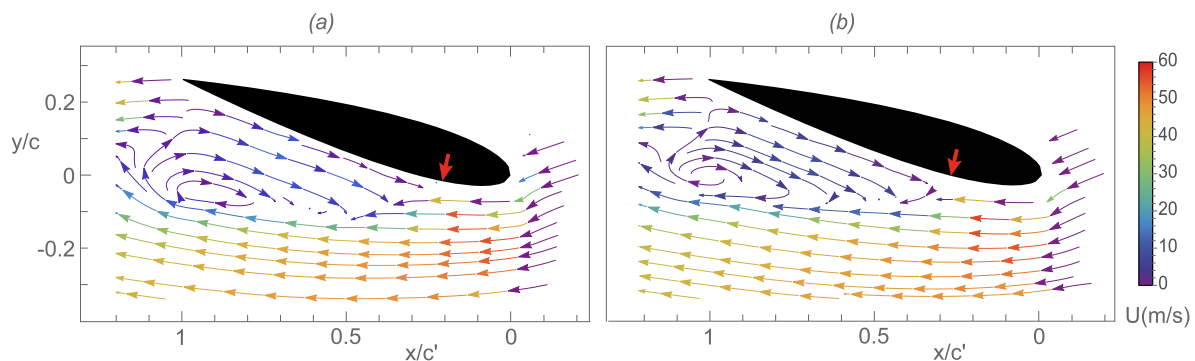

Figure 14. (**a**) Plasma-off and (**b**) plasma-on flow field at T_A for $\alpha = 14.5°$ and $U_\infty = 35$ m/s.

After these validations, the study proceeded with the analysis of the spanwise sections, performed at an intermediate velocity of $U_\infty = 30$ m/s, as anticipated in Section 2.

3.2. Spanwise Sections Analysis at $U_\infty = 30$ m/s, $\alpha = 14.5°$

After the setup and actuator authority validation, the actuator effect on the five spanwise sections at $U_\infty = 30$ m/s and $\alpha = 14.5°$ was analyzed. Since the tip-root difference was already examined in Section 3.1, the measures were performed on the five tip planes T_A, T_B, T_C, T_D, T_E, reported in Figure 7. During these tests, the cameras were kept fixed, so they captured wider flow fields in correspondence with the outer sections. Therefore, all the images collected for the lateral planes needed to be corrected for the perspective effect through a rescaling.

Once again, the central sections were analyzed first. The study of tip T_A in the plasma-off configuration (Figure 15a) shows separation at about 20% of the chord whilst the recirculation bubble is extended up to the trailing edge. When the actuator is turned on (Figure 15b) it has a good authority on the flow, leading to a shift in the separation point of about $0.1c$ and to a reduction of the recirculation

bubble, diminishing its extension and displacing its center closer to the airfoil. Accordingly, the outer streamlines are deflected toward the airfoil, presumably leading to a decrease of the pressure coefficient and consequently to a lift increase.
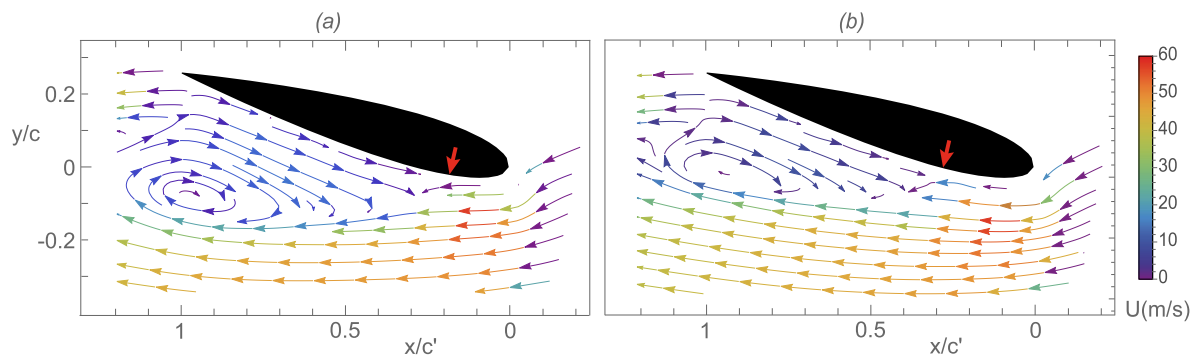

Figure 15. (**a**) Plasma-off and (**b**) plasma-on flow field at T_A for $\alpha = 14.5°$ and $U_\infty = 30$ m/s.

Moving along the span, the next examined tip is T_B. The plasma-off condition is reported in Figure 16a, where a natural displacement of the separation point toward the trailing edge is already observed due to the classical three-dimensional flow geometry over the finite wing. Under the plasma effect (Figure 16b) a further shift in the order of 0.1 c is measured, along with a reduction of the recirculation bubble of which the center lays closer to the airfoil. At the same time, the external streamlines are accelerated and deflected closer to the airfoil. Then, even if the three-dimensional flow geometry pushes the natural separation point downstream of the actuator tip position, the actuator still has a good authority on the flow with beneficial effects for the wing performance.
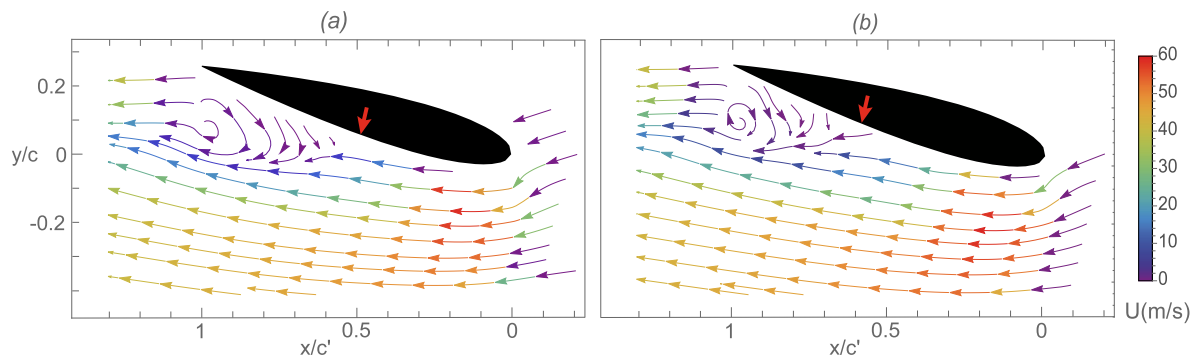

Figure 16. (**a**) Plasma-off and (**b**) plasma-on flow field at T_B for $\alpha = 14.5°$ and $U_\infty = 30$ m/s.

A similar flow field is encountered at T_C, with the separation point in the plasma-off configuration already laying within 50% of chord from the trailing edge (Figure 17a) With plasma on (Figure 17b) it is further shifted downstream, influencing a narrower region of the flow. The streamlines are again accelerated and realigned with the airfoil profile, presumably enhancing the lift coefficient also at this station.
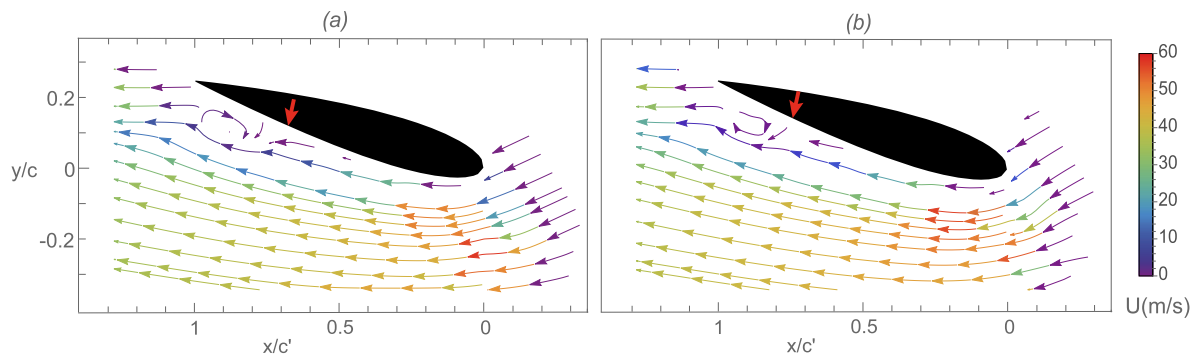
Figure 17. (**a**) Plasma-off and (**b**) plasma-on flow field at T_C for $\alpha = 14.5°$ and $U_\infty = 30$ m/s.

Finally, tips T_D and T_E were examined: these plasma-off configurations (Figures 18a and 19a) are nearly or completely attached, yet the plasma effect is still slightly visible from the mild acceleration of the streamlines (Figures 18b and 19b). Howeverm the local flow is close to being independent from actuator activation. This suggests that an electrode of lower span, obtained removing the tips corresponding to the lateral flow sections, could have very similar flow control capabilities on the whole wing, requiring a lower power consumption.
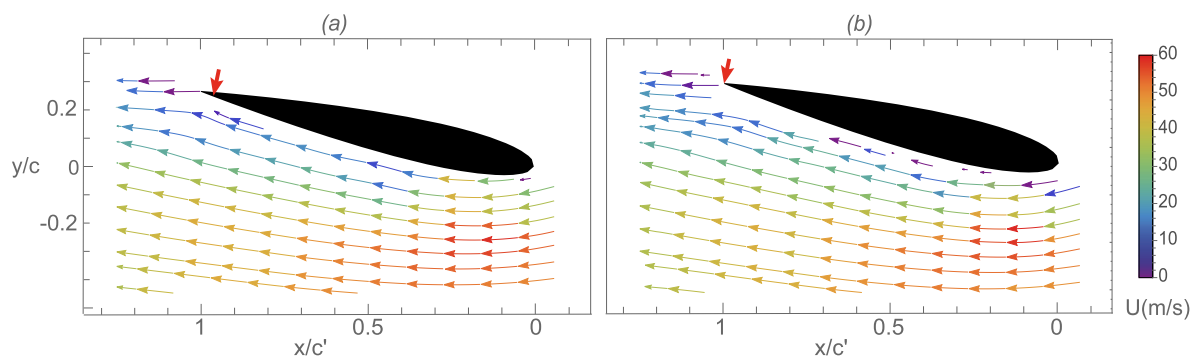

Figure 18. (**a**) Plasma-off and (**b**) plasma-on flow field at T_D for $\alpha = 14.5°$ and $U_\infty = 30$ m/s.
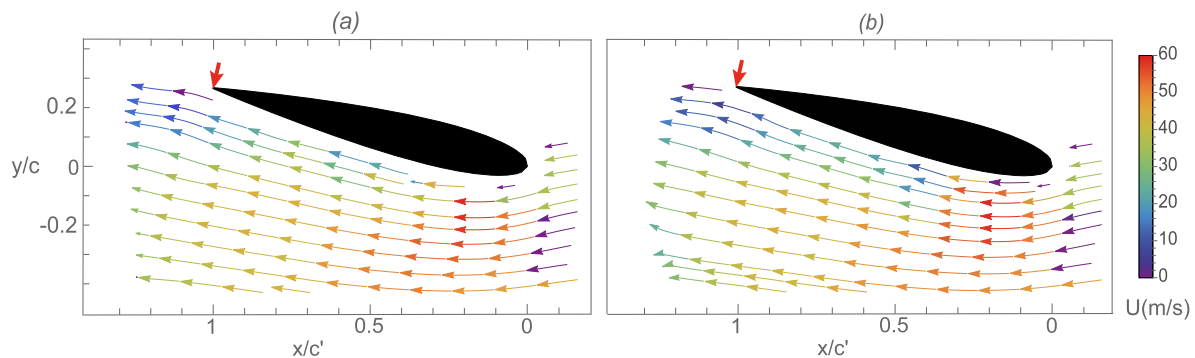

Figure 19. (**a**) Plasma-off and (**b**) plasma-on flow field at T_E for $\alpha = 14.5°$ and $U_\infty = 30$ m/s.

As was done for the $U_\infty = 20$ m/s study, also here, the cross-wake velocity and C_P were computed to confirm the actuator effects on the flow. The cross-wake velocity profiles reported in Figure 20 were computed, as before, along a vertical axis located $c/6 = 50$ mm from the trailing edge. Since the last two PIV planes T_D and T_E show similar characteristics, only the T_E profile is shown. The effect of the three-dimensional flow geometry is again visible: the momentum drop in the plasma-off configuration is progressively reduced both in magnitude and extension moving towards the lateral sections. Despite this, on the central sections, a significant further reduction can be observed in the plasma-on case, confirming the actuator authority. Similarly, also the lateral regions

show some slight changes in the actuated velocity profiles, mainly related to a wake reduction effect. The actuator-flow interaction, then, seems to be beneficial on all the tested planes.
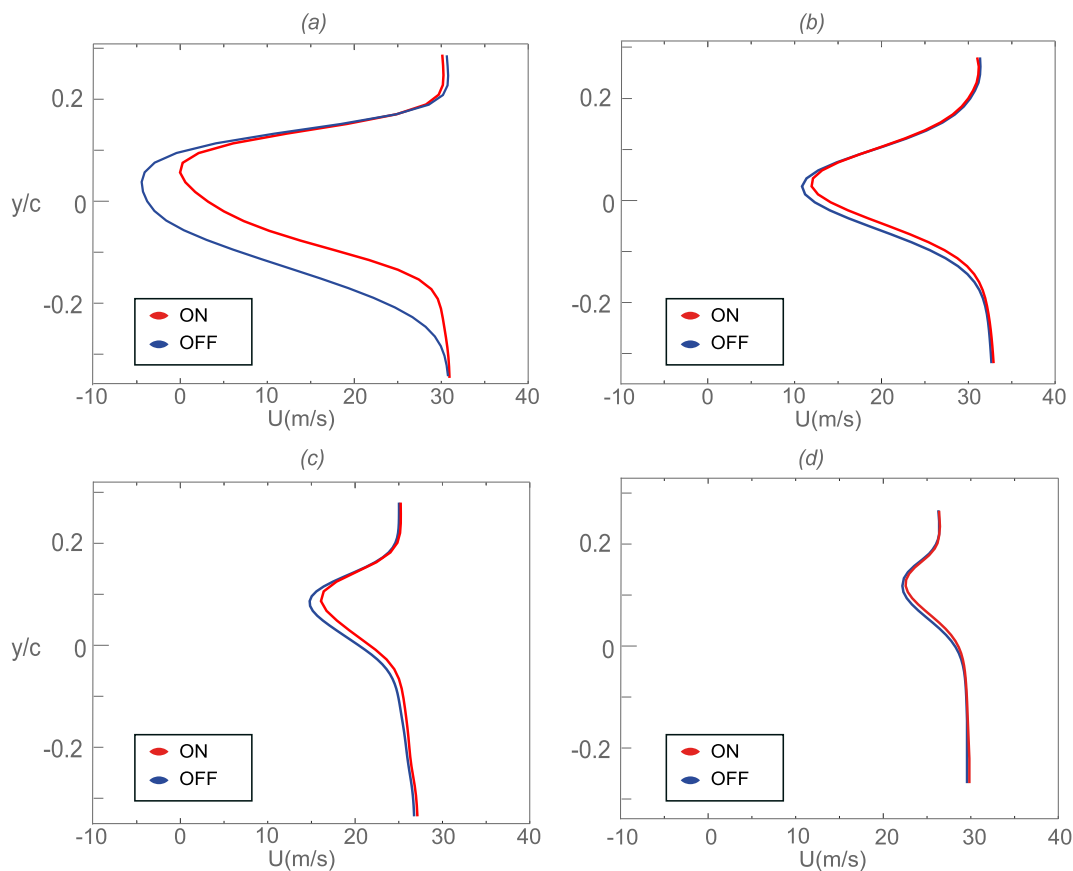

Figure 20. Cross-wake velocity profiles at (**a**) T_A, (**b**) T_B, (**c**) T_C, and (**d**) T_E for $\alpha = 14.5°$ and $U_\infty = 30$ m/s.

With the same procedure described in Section 3.1, the off–on variations in the C_P curves were evaluated for different spanwise sections. These data are reported in Figure 21 for the planes T_A, T_B, T_C, confirming that the main region of influence lies in the central zone of the model. In particular, the plasma effect leads to a significant increase of the C_P peak value in the central section T_A, where it grows about 30%; then, the off–on difference is progressively reduced moving toward the lateral planes. However, the chordwise extension of the region influenced by the actuator increases on the lateral planes, so that it is reasonable to expect a contribution on the total lift from all the studied sections.
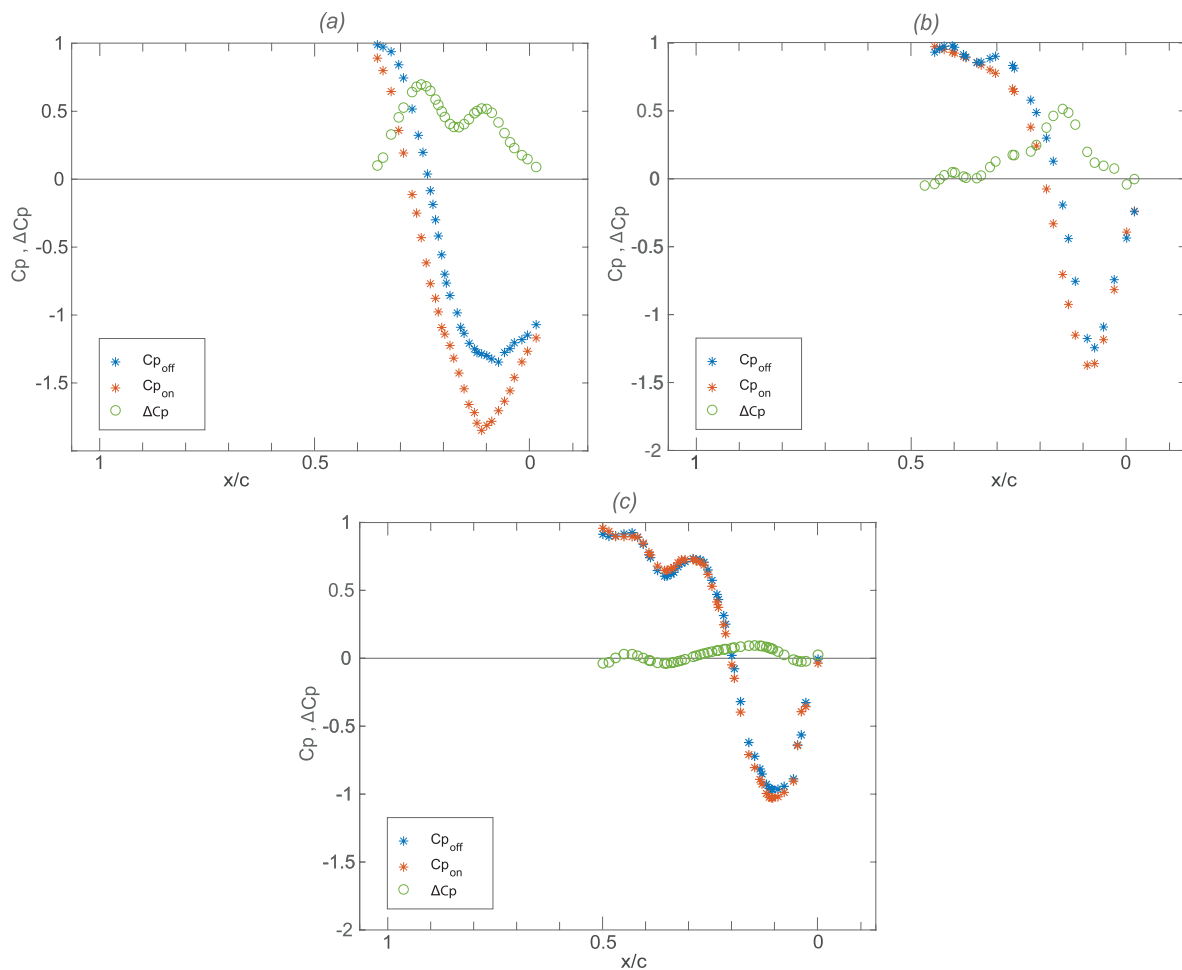
Figure 21. C_P values at (**a**) T_A, (**b**) T_B, and (**c**) T_C for $\alpha = 14.5°$ and $U_\infty = 30$ m/s.

With a further elaboration of the PIV data, the location and displacement of the separation points has been estimated for all the analyzed sections. This allowed to obtain a representation of the complete three-dimensional separation line over the whole airfoil span both for plasma-on and -off configurations, as reported in Figure 22 and Table 1. A more refined scan, based on a large number of PIV planes, would lead to a similar shape but includes a superimposed undulation, which is due to the tip-root differences previously described. The plasma-off separation line (blue line in figure) shows the classical contour for a finite wing [23,25]; that is expected to appear also in a wind tunnel test if, as in this experiment, large end plates are not introduced. Under the actuator effect, the separation line (red line) retains a very similar shape but is completely shifted downstream. This displacement may seem mild, but the involved area is quite wide and affects a region where the pressure changes on the model surface can lead to a significant lift variation. Further studies could be done investigating possible enhancements of the control authority: after optimizing the actuator for a given airspeed (Section 2) and setting the same supply to avoid an increase of power consumption, there is the chance to change the DBD location, keeping in mind that the actuation must always take place upstream of the separation, as proven in Reference [33,34]. This would lead to placing the actuator upstream around the airfoil nose, affecting the flow also in the accelerated zone between the stagnation and the nose itself, and could give rise to further developments.
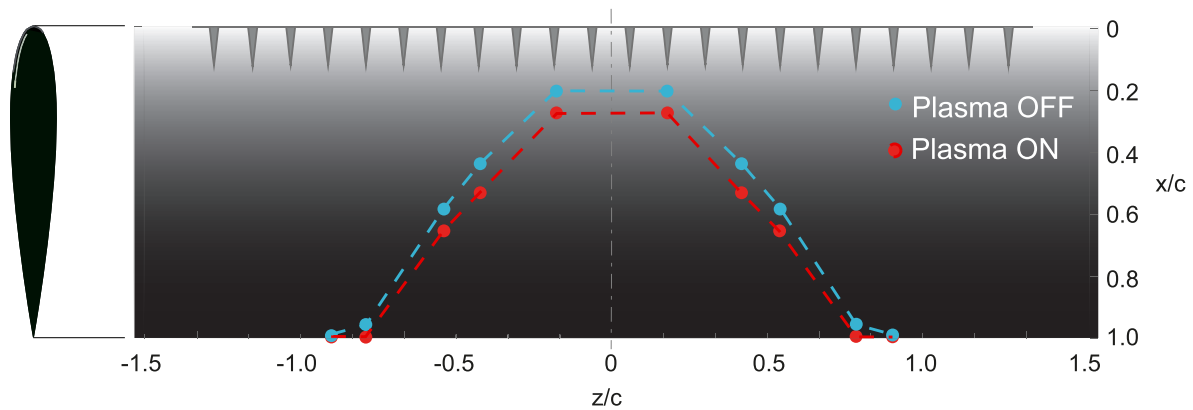
Figure 22. Sketch of the separated region for $\alpha = 14.5°$ and $U_\infty = 30$ m/s.

Finally, Figure 22 also shows that, in the outer tested sections, the plasma-on and -off separation points coincide or are very close to each other, indicating that even if the actuator influences the flow over the whole wing, its major effects are on the central sections. Therefore, removing the outer tips of the exposed electrode (the ones corresponding to the already attached flow sections) may lead to a similar overall performance, reducing the power consumption of the DBD device.

Table 1. Off-to-on chordwise shift of separation vs. spanwise position z: The origin is at the intersection of leading edge and tunnel centerline.

PIV Plane	Spanwise Position			Separation Shift	
	(mm)	(z/c)	(z/S)	(mm)	(x/c)
T_A	54.0	0.18	0.058	22.0	0.073
T_B	126.0	0.42	0.135	28.0	0.093
T_C	162.0	0.54	0.174	20.0	0.067
T_D	234.0	0.78	0.252	9.0	0.030
T_E	270.0	0.90	0.290	0.0	0.000

3.3. Actuator Effectiveness

In the previous sections, some three-dimensional results were presented through the analysis of the separation line. In particular, this allowed to observe that the separated region sensitive to the actuator effect lies in the central part of the model. Instead, the lateral sections are only marginally influenced, suggesting that two electrodes of shorter span can presumably give a similar overall effect requiring lower power, thus improving the device efficiency. Recalling that the passive effects of the actuator are weak, the flow field over the whole model can be considered to remain almost the same with a shorter DBD. The original actuator has 22 tips, and the results analysis suggests to remove 8 of them, corresponding to the 4 outer ones on each side over which the flow is attached. In this way, the actuator length and power consumption would diminish up to 36%, namely the initial $W_0 = 167$ W read in bench tests (Section 2) would be lowered to $W_1 = 106$ W.

To determine the capabilities of the actuator in a realistic application, it is desirable to compare the power consumption W with the variations of aerodynamics forces and useful power. Considering the possible effects of lift increase ΔL and drag reduction ΔD, two effectiveness parameters $\Delta L/W$ and $\Delta D/W$ could be introduced, with dimension N/W. Correspondingly, two dimensionless efficiencies could be formally introduced: (1) by considering a wing lifting a given load with vertical velocity V_t, the lifting power is $L V_t$ and the (lifting power increment)/(electric power) ratio is $\Delta L V_t/W$; (2) considering the drag reduction, the corresponding (power saving)/(electric power) ratio is $\Delta D U_\infty/W$.

The complete determination of the above parameters would require values of lift and drag, with the drag typically affected by a larger uncertainty. These forces are not directly readable

with the present setup; however, a simplified study can be done by considering only the lift increase ΔL. Assuming, as exposed above, a negligible variation of ΔL between the two configurations (long and short DBD), the effectiveness $\epsilon = \Delta L/W$ would change from $\epsilon_0 = \Delta L/W_0$ to $\epsilon_1 = \Delta L/W_1$ for a shorter actuator, with an improvement $\epsilon_1/\epsilon_0 = 1.57$, regardless of the ΔL value.

Moreover, a rough estimate of the ΔL value can be obtained by the variations of the C_P coefficients presented in the previous section, accounting for the known properties of the 0015 airfoil. With steady actuation at $U_\infty = 30$ m/s and $\alpha = 14.5°$, it is obtained an approximate value of 15 N over the whole wing. With this value, the effectiveness ratio $\epsilon_0 = \Delta L/W_0$ turns out to be about 0.09 N/W, and the corresponding dimensionless efficiency is $\eta_0 = 0.09\, V_t$. Clearly, in a practical application, this efficiency must be higher than one, and the relation $\eta_0 > 1$ shows that the present model would need a minimum ascent velocity $V_t \simeq 11.1$ m/s to operate properly. More favourably, the condition $\eta_1 = \Delta L\, V_t/W_1 > 1$ referred to as a shorter actuator with lower power W_1 would reduce the minimal ascent velocity to $V_t \simeq 7.1$ m/s. A further improvement could be achieved by using a pulsed actuation with reduced frequency $F_+ = 1$ and high duty cycle of 80%, since this combination has been proven to control the stall inception with performance very similar to the steady actuation (duty cycle 100%), with the advantage of saving 20% of power [20]. The minimal ascent velocity would be lowered in this case to about 5.7 m/s.

This indicates that the technology level is appropriate for realistic applications, since the minimal ascent velocities above are lower than the rates of climb of several diffused light aircrafts under full load, as for example Lancair IV-P (10 to 15 m/s for different versions), Pipistrel Virus 912 SW100 (8.4 m/s), de Havilland DHC-6 (8.1 m/s), Cessna 400 (7.6 m/s), and Cirrus SR 22 (6.6 m/s). Of course, further study would be needed for each aircraft, including the evaluation of drag and accounting for their specific characteristics as wing profile, takeoff and climb performance, and the other important V-speeds.

4. Conclusions and Further Developments

This study characterizes the effect of a multi-tip DBD actuator over a wing, consisting of an airfoil model considered as a three-dimensional body and thus intentionally placed in the wind tunnel without end-plates. Through PIV measurements, five spanwise distributed sections were studied, from the model centerline to the external section.

Several tests have been run under different stall conditions: in general, the actuator-flow interaction takes place along the whole span of the model but the local effects are different, depending on the corresponding base flow. In particular, in early stall conditions, the base flow along the central section of the model is separated whereas it remains attached on the external regions. Correspondingly, the plasma discharge acts in different ways: in the central zone, it reduces the recirculating region size and shifts the separation points downstream, whereas on the external sections, it only induces slight modifications of the local streamlines. This suggests that an actuator of shorter span, with a corresponding lower power consumption, could achieve a similar separation control: assuming that the global effect of the actuator remains unaltered, the effectiveness measured in terms of N/W can increase in this way up to 57%.

Finally, as regards plasma flow control experiments on airfoils, it is concluded that the validity of data collected near the centerline should be considered local, unless end/splitter plates of proper size are installed to counteract and limit the natural three-dimensional structure of the flow.

Nomenclature

c, c'	airfoil chord and projection $c \cos \alpha$, m
C_L	lift coefficient
C_P	pressure coefficient
d	spacing of DBD tips, mm
D	drag, N
f	DBD carrier frequency, Hz
F, F_+	DBD modulation frequency: dimensional, Hz, and dimensionless
h	length of DBD tips, mm
L	lift, N
Re	Reynolds number
r	tips sharpness h/w
S	airfoil span, m
T_C	convective time scale along a tip, s
T_ν	viscous time scale along a tip, s
T_R	recirculation time scale between tips, s
U_∞	freestream velocity, m/s
V_i	ionic wind velocity, m/s
V_t	vertical ascent velocity or rate of climb, m/s
w	width of DBD tips, mm
W	electrical power, W
x, y, z	chordwise, normal and spanwise coordinates, m
α	angle of attack, °
ϵ	DBD effectiveness in lift increase, N/W
η	dimensionless DBD efficiency in lift increase

References

1. Moreau, E. Airflow control by non-thermal plasma actuators. *J. Phys. D Appl. Phys.* **2007**, *40*, 605. [CrossRef]
2. Benard, N.; Moreau, E. Electrical and mechanical characteristics of surface AC dielectric barrier discharge plasma actuators applied to airflow control. *Exp. Fluids* **2014**, *55*, 1846. [CrossRef]
3. Kriegseis, J.; Simon, B.; Grundmann, S. Towards in-flight applications? A review on dielectric barrier discharge-based boundary-layer control. *Appl. Mech. Rev.* **2016**, *68*, 1–41. [CrossRef]
4. Kotsonis, M. Diagnostics for characterisation of plasma actuators. *Measur. Sci. Technol.* **2015**, *26*, 092001. [CrossRef]
5. Kelley, C.L.; Corke, T.C.; Thomas, F.O.; Patel, M.; Cain, A.B. Design and scaling of plasma streamwise vortex generators for flow separation control. *AIAA J.* **2016**, *11*, 3397–3408. [CrossRef]
6. He, C.; Corke, T.C.; Patel, M.P. Plasma flaps and slats: An application of weakly ionized plasma actuators. *J. Aircr.* **2009**, *46*, 864–873. [CrossRef]
7. Kelley, C.; Bowles, P.; Cooney, J.; He, C.; Corke, T.; Osborne, B.; Silkey, J.; Zehnle, J. High mach number leading-edge flow separation control using AC DBD plasma actuators. In Proceedings of the 50th AIAA Aerospace Sciences Meeting Including the New Horizons Forum and Aerospace Exposition, Nashville, TN, USA, 9–12 January 2012; p. 906.
8. Benard, N.; Braud, P.; Jolibois, J.; Moreau, E. Airflow reattachment along a NACA 0015 airfoil by surfaces dielectric barrier discharge actuator: Time-resolved particle image velocimetry investigation. In Proceedings of the 4th Flow Control Conference, Seattle, WA, USA, 23–26 June 2008; p. 4202.
9. Joussot, R.; Hong, D.; Weber-Rozenbaum, R.; Leroy-Chesneau, A. Modification of the laminar-to-turbulent transition on a flat plate using DBD plasma actuator. In Proceedings of the 5th Flow Control Conference, Chicago, IL, USA, 28 June–1 July 2010; p. 4708.
10. Sekimoto, S.; Nonomura, T.; Fujii, K. Burst-mode frequency effects of dielectric barrier discharge plasma actuator for separation control. *AIAA J.* **2017**, *55*, 1385–1392. [CrossRef]
11. Bénard, N.; Jolibois, J.; Moreau, E. Lift and drag performances of an axisymmetric airfoil controlled by plasma actuator. *J. Electrost.* **2009**, *67*, 133–139. [CrossRef]

12.   Kelley, C.L.; Bowles, P.O.; Cooney, J.; He, C.; Corke, T.C.; Osborne, B.A.; Silkey, J.S.; Zehnle, J. Leading-edge separation control using alternating-current and nanosecond-pulse plasma actuators. *AIAA J.* **2014**, *52*, 1871–1884. [CrossRef]

13.   Corke, T.; Mertz, B.; Patel, M. Plasma flow control optimized airfoil. In Proceedings of the 44th AIAA Aerospace Sciences Meeting and Exhibit, Reno, NV, USA, 9–12 January 2006; p. 1208.

14.   Thomas, F.O.; Corke, T.C.; Iqbal, M.; Kozlov, A.; Schatzman, D. Optimization of dielectric barrier discharge plasma actuators for active aerodynamic flow control. *AIAA J.* **2009**, *47*, 2169. [CrossRef]

15.   Forte, M.; Jolibois, J.; Pons, J.; Moreau, E.; Touchard, G.; Cazalens, M. Optimization of a dielectric barrier discharge actuator by stationary and non-stationary measurements of the induced flow velocity: Application to airflow control. *Exp. Fluids* **2007**, *43*, 917–928. [CrossRef]

16.   Wang, C.C.; Durscher, R.; Roy, S. Three-dimensional effects of curved plasma actuators in quiescent air. *J. Appl. Phys.* **2011**, *109*, 083305. [CrossRef]

17.   Belan, M.; Messanelli, F. Compared ionic wind measurements on multi-tip corona and DBD plasma actuators. *J. Electrost.* **2015**, *76*, 278–287. [CrossRef]

18.   Messanelli, F.; Belan, M. Ionic wind measurements on multi-tip plasma actuators. In Proceedings of the EFM15—Experimental Fluid Mechanics 2015, Prague, Czech Republic, 17–20 November 2015; pp. 1–8.

19.   Messanelli, F.; Belan, M. A comparison between corona and DBD plasma actuators for separation control on an airfoil. In Proceedings of the 55th AIAA Aerospace Sciences Meeting, Grapevine, TX, USA, 9–13 January 2017; p. 0395.

20.   Messanelli, F.; Frigerio, E.; Tescaroli, E.; Belan, M. Separation control by plasma actuators: Effects of direct momentum injection and vortex generation. *Flow Turbulence Combust.* **2019**. [CrossRef]

21.   Zoppini, G.; Di Vinci, L.; Campanardi, G.; Zanotti, A.; Belan, M. PIV characterization of a separated flow controlled by a DBD actuator. In Proceedings of the XXVI AIVELA National Meeting, Milano, Italy, 29–30 November 2018; pp. 1–13.

22.   Corke, T.; Enloe, C.; Wilkinson, S. Dielectric barrier discharge plasma actuators for flow control. *Ann. Rev. Fluid Mech.* **2010**, *42*, 505–529. [CrossRef]

23.   Winkelmann, A. Flow field studies behind a wing at low reynolds numbers. In Proceedings of the AIAA 21st Fluid Dynamics, Plasma Dynamics and Lasers Conference, Seattle, WA, USA, 18–20 June 1990; pp. 1–18.

24.   Winkelmann, A.; Barlow, J. A flowfield model for a rectangular planform wing beyond stall. *AIAA J.* **1980**, *18*, 1006–1008. [CrossRef]

25.   Boiko, A.; Dovgal, A.; Zanin, B.; Kozlov, V. Three-dimensional structure of separated flows on wings (review). *Thermophys. Aeromech.* **1996**, *3*, 1–13.

26.   Wicks, M.; Thomas, F.O.; Corke, T.C.; Patel, M.; Cain, A.B. Mechanism of vorticity generation in plasma streamwise vortex generators. *AIAA J.* **2015**, *53*, 3404–3413. [CrossRef]

27.   Belan, M.; Messanelli, F. Wind tunnel testing of multi-tip corona actuators on a symmetric airfoil. *J. Electrost.* **2017**, *85*, 23–34.

28.   Messanelli, F.; Frigerio, E.; Tescaroli, E.; Belan, M. Flow separation control by pulsed corona actuators. *Exp. Therm. Fluid Sci.* **2019**, *105*, 123–135. [CrossRef]

29.   Messanelli, F. Optimization of plasma actuators for flow control. Ph.D. Thesis, Politecnico di Milano, Milano, Italy, 2017. [CrossRef]

30.   Kriegseis, J.; Grundmann, S.; Tropea, C. Performance reduction of dielectric barrier discharge plasma actuators at higher mach numbers. In *New Results in Numerical and Experimental Fluid Mechanics VIII*; Springer: Berlin/Heidelberg, Germany 2013; pp. 209–217. [CrossRef]

31.   Jukes, T.N.; Choi, K.S. On the formation of streamwise vortices by plasma vortex generators. *J. Fluid Mech.* **2013**, *733*, 370–393.

32.   Auteri, F.; Carini, M.; Zagaglia, D.; Montagnani, D.; Gibertini, G.; Merz, C.; Zanotti, A. A novel approach for reconstructing pressure from PIV velocity measurements. *Exp. Fluids* **2015**, *56*, 45.

33. Jolibois, J.; Forte, M.; Moreau, E. Application of an AC barrier discharge actuator to control airflow separation above a NACA 0015 airfoil: Optimization of the actuation location along the chord. *J. Electrost.* **2008**, *66*, 496–503. [CrossRef]

34. Tsubakino, D.; Tanaka, Y.; Fujii, K. Effective layout of plasma actuators for a flow separation control on a wing. In Proceedings of the 45th AIAA Aerospace Sciences Meeting and Exhibit, Reno, NV, USA, 8–11 January 2007; pp. 1–18. [CrossRef]